nature communications

Article

https://doi.org/10.1038/s41467-024-54601-7

Pd hydride metallene aerogels with lattice hydrogen participation for efficient hydrogen evolution reaction

Received: 25 March 2024

Accepted: 15 November 2024

Published online: 27 November 2024

Check for updates

Hengjia Wang[1], Ying Qin[1], Yu Wu[1], Yiwei Qiu[1], Ling Ling[1], Qie Fang[1], Canglong Wang[2], Liuyong Hu[3], Wenling Gu[1] & Chengzhou Zhu[1]

Hydrogen adsorption and desorption in single-phase catalysts often occur at a single catalytic site based on the traditional hydrogen evolution reaction (HER) pathway, which makes it difficult to break the limitation entailed by the Sabatier principle. Herein, β-Pd hydride metallene (β-PdHene) aerogels are synthesized as advanced HER catalysts. A lattice hydrogen-involved mechanism is reported to separate adsorption and desorption sites, which is thermodynamically favorable compared to the traditional reaction pathway. In situ differential electrochemical mass spectrometry and theoretical calculations reveal that lattice hydrogen as additional active sites directly participate in the HER process. Consequently, β-PdHene aerogels exhibit a low overpotential of only 20 mV at 10 mA cm^{-2} and remarkable HER stability, which are even comparable to commercial Pt/C. Our work opens an avenue to rationally develop highly active HER catalysts, bypassing the design limitations of catalysts under traditional mechanisms.

Hydrogen (H_2) is considered an ideal alternative to substitute traditional fossil fuels and is also a key feedstock for key industrial products because of its high energy density and zero carbon emissions, which meet the requirement of global carbon neutrality[1–6]. The electrocatalytic hydrogen evolution reaction (HER) is one of the most attractive and economical methods of high-quality H_2 production[7–9]. The Pt-based nanomaterials are widely reported as the most efficient electrocatalysts[10–12]. Owing to the similar electronic structure and the high abundance, Pd-based catalysts as the alternatives have attracted great attention[13]. However, the strong binding between Pd and H is not conducive to H_2 desorption, resulting in inferior HER performance[14,15]. Therefore, constructing advanced HER electrocatalysts is highly desirable, yet challenging for a green hydrogen economy.

Insights on the catalytic HER mechanism of catalysts are of great significance for maximizing the efficiency of electrocatalysts. Currently, the acid HER pathway typically involves the Volmer step, which generates adsorbed hydrogen intermediates (H*) by electrochemical reduction, generally followed by either the charge-transfer Heyrovsky process ($H^* + e^- + H^+ \rightarrow H_2$) or a Tafel recombination process ($H^* + H^* \rightarrow H_2$) to produce H_2[16,17]. The efficiency of HER electrocatalysts under an acidic medium depends largely on the balance of hydrogen adsorption/desorption behavior on the catalyst surface. Based on the Sabatier principle, an ideal HER electrocatalyst presents near-zero hydrogen adsorption-free energy (ΔG_{H^*})[18]. Too strong or too weak of hydrogen binding ability can result in either poisoning of active sites or inefficient proton supplement, greatly decreasing the reaction kinetics of HER[19,20]. Moreover, the hydrogen adsorption and desorption in single-phase catalysts usually happen at a single active site according to the traditional HER mechanism, which makes it hard to overcome the limitations of the Sabatier principle. Consequently, exploring advanced electrocatalysts is expected to achieve multiple catalytic sites and break the bottleneck of the existing HER mechanism.

Herein, we proposed a lattice hydrogen-involved mechanism to separate the adsorbing and desorbing sites on β-Pd hydride metallene

[1]State Key Laboratory of Green Pesticide, International Joint Research Center for Intelligent Biosensing Technology and Health, College of Chemistry, Central China Normal University, Wuhan, P. R. China. [2]Institute of Modern Physics, Chinese Academy of Science, Lanzhou, P. R. China. [3]Hubei Key Laboratory of Plasma Chemistry and Advanced Materials, Hubei Engineering Technology Research Center of Optoelectronic and New Energy Materials, Wuhan Institute of Technology, Wuhan, P. R. China. e-mail: czzhu@ccnu.edu.cn

(β-PdHene) aerogels to boost HER performance in acidic media, which has more favorable thermodynamics than the traditional reaction pathway. In situ differential electrochemical mass spectrometry (DEMS) test and density functional theory (DFT) offer solid evidence for the participation of lattice hydrogen during HER. The neighboring H* migrates and combines with the revitalized lattice hydrogen on the surface into H_2, facilitating H_2 desorption. Specifically, a notably small overpotential of only 20 mV of β-PdHene aerogels is achieved at 10 mA cm^{-2}, as well as good stability. The distinct roles of lattice hydrogen participation of Pd hydride metallene for HER were revealed, allowing us to better understand the overall HER mechanism.

Results

Synthesis and characterization of β-PdHene aerogels

β-PdHene gels were prepared by the two-step method as schematically illustrated in Fig. 1a. Initially, the Pd metallene (Pdene) gels were synthesized by a CO-mediated gelation strategy. Hydrogen insertion is achieved under solvothermal conditions in dimethylformamide (DMF)[21]. Subsequently, β-PdHene gels were gained by in situ insertion of hydrogen atoms formed from the decomposition of DMF on Pdene gels at 160 °C. After further purification and supercritical CO_2 drying, monolithic β-PdHene aerogels were obtained (inset in Fig. 1b). Scanning electron microscopy (SEM) image reflects the hierarchically porous structure of the resulting β-PdHene aerogels (Fig. 1b). High-angle annular dark-field scanning transmission electron microscopy (HAADF-STEM) and transmission electron microscopy (TEM) images of β-PdHene aerogels display a thin and wrinkled two-dimensional (2D) graphene-like morphology with an average lateral dimension of up to several hundred nanometers (Fig. 1c, d). The selected-area electron diffraction (SAED) pattern shows the polycrystalline structure of the β-PdHene aerogels (inset in Fig. 1d). The thickness of β-PdHene aerogels is measured to about 1.26 nm by atomic force microscopy (AFM),

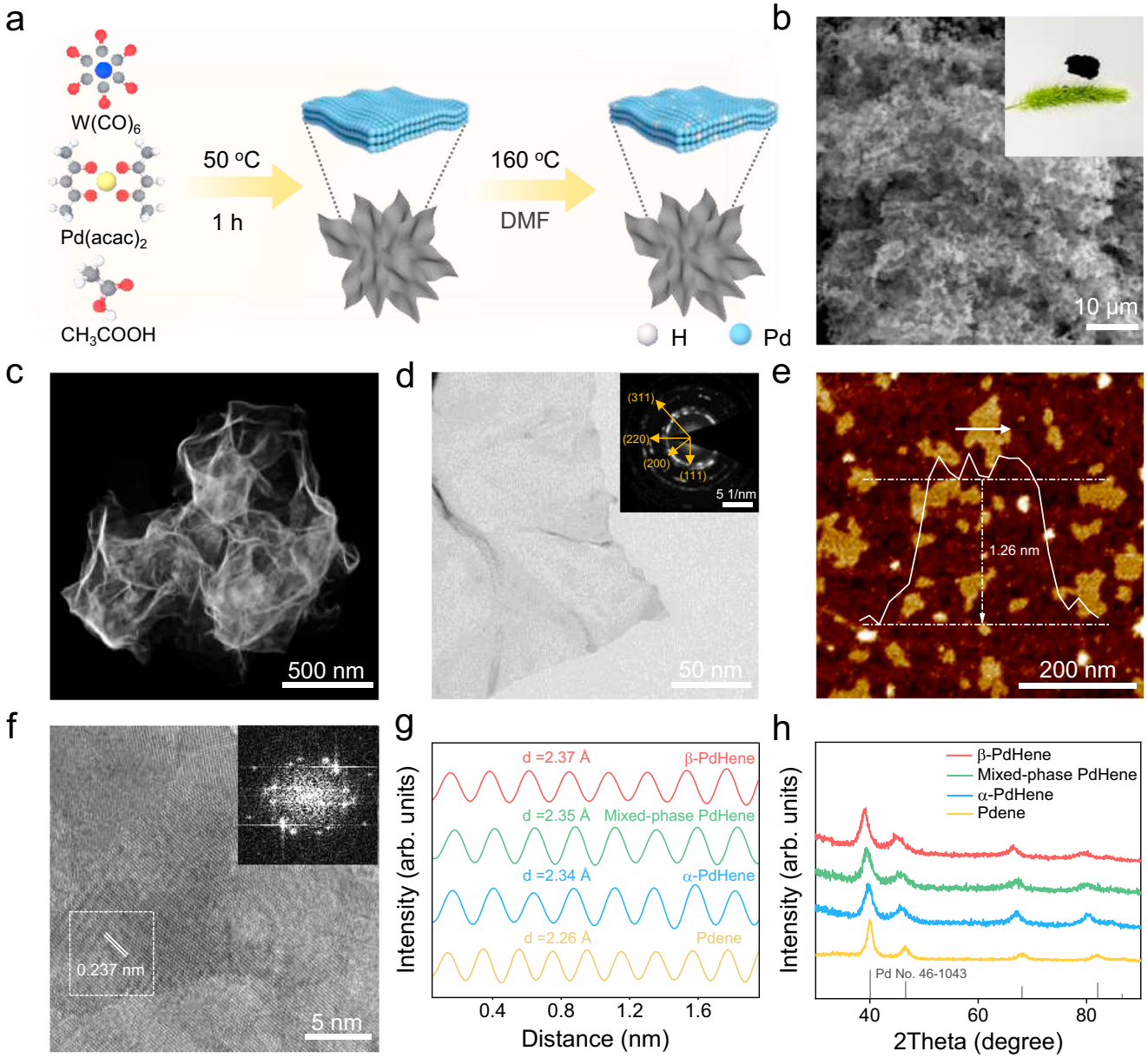

Fig. 1 | Synthesis and characterization of β-PdHene aerogels. a Schematic illustration for the synthesis of β-PdHene gels. **b** SEM image, (**c**) HAADF-STEM image, (**d**) TEM image, (**e**) AFM image and corresponding height profiles, and (**f**) HRTEM image of β-PdHene aerogels. Inset in **b**, **d**, and (**f**) shows the digital photo, SAED pattern, and corresponding FFT pattern of β-PdHene aerogels, respectively. Integrated pixel intensity profiles (**g**) and XRD patterns (**h**) of Pdene and different phases of PdHene aerogels. Source data for Fig. 1 are provided as a Source Data file.

equivalent to 5–6 atomic layers, which further validates the thin feature (Fig. 1e). The high-resolution TEM (HRTEM) image and the corresponding fast Fourier transform (FFT) pattern suggest the β-PdHene aerogels present a (111)-oriented face-centered cubic (fcc) structure. Distinct lattice spacing of 0.237 nm can be attributed to the (111) planes (Fig. 1f)[22,23]. The surface areas and porosity features of Pdene and β-PdHene aerogels were evaluated by the Brunauer-Emmett-Teller (BET) analysis (Supplementary Fig. S1). The surface area of β-PdHene aerogels (48.9 $m^2 g^{-1}$) is slightly smaller than that of Pdene (64.7 $m^2 g^{-1}$), which may be caused by the subsequent in situ insertion of hydrogen atoms at 160 °C. The wide existence of micropores, mesopores, and macropores within β-PdHene and Pdene aerogels was observed, which facilitates mass/electron transfer. The α-PdHene and mixed-phase PdHene aerogels were also obtained by a similar method at 120 °C and 140 °C, respectively. Pdene, α-PdHene, and mixed-phase PdHene aerogels show similar highly porous three-dimensional networks and few-layer thin nanosheet morphology (Supplementary Figs. S2–S4). The metallene feature of α-PdHene and mixed-phase PdHene aerogels can be also measured by AFM, which exhibits a thickness of 1.24 nm and 1.3 nm in Supplementary Fig. S5, respectively. As shown in Fig. 1g, the average lattice distance in the β-PdHene aerogels is measured to be 2.37 Å, which is much larger than those of Pdene (2.26 Å), α-PdHene (2.34 Å) and mixed-phase PdHene (2.35 Å). The expanded lattice distance also shows that the alloyed hydride metallene is successfully prepared. The X-ray diffraction (XRD) pattern shows that the more negatively the diffraction peaks shift, the more hydrogen atoms are inserted with the reaction temperature increasing from 120 °C to 160 °C (Fig. 1h). In addition, according to Eqs. 2–4, the lattice parameters and compositions of Pdene and different phases of PdHene aerogels are displayed in Supplementary Table S1. The H and Pd ratio in the α-PdHene, mixed-phase PdHene, and β-PdHene aerogels is calculated to be 0.08, 0.28, and 0.43, respectively. The interaction between Pd and hydrogen atoms was analyzed by X-ray photoelectron spectroscopy (XPS) valence band spectra in Supplementary Fig. S6. The narrowing of the half-band width (from 4.53 eV to 4.14 eV) manifests the electronic structure changes owing to a larger Pd-Pd distance in the hydride[24–26]. Importantly, the β-PdHene aerogels own good storage stability and can be stored for at least 12 months in an air environment without damaging the structure (Supplementary Fig. S7).

Electrocatalytic HER performance

The electrocatalytic HER activity of Pdene, different phases of PdHene aerogels, and commercial Pt/C was estimated at a rotating disk electrode under 1600 rpm with N_2-saturated 0.5 M H_2SO_4 as electrolyte (Fig. 2a and Supplementary Fig. S8). Surprisingly, β-PdHene aerogels possess overpotentials of only 20 and 66 mV at the current density of 10 mA cm^{-2} and 50 mA cm^{-2} (Fig. 2b), which are lower than those of Pdene (η_{10} = 56 mV, η_{50} = 131 mV) and commercial Pt/C (η_{10} = 32 mV, η_{50} = 87 mV). Moreover, the overpotential of β-PdHene aerogels at different current densities shows a much smaller value than those of mixed-phase PdHene aerogels (η_{10} = 36 mV, η_{50} = 95 mV) and α-PdHene (η_{10} = 52 mV, η_{50} = 120 mV). As depicted in Fig. 2c, the Tafel slope of β-PdHene aerogels is 37.8 mV dec^{-1}, surpassing Pdene (97.6 mV dec^{-1}), Pt/C (40.5 mV dec^{-1}), mixed-phase PdHene (52.7 mV dec^{-1}) and α-PdHene aerogels (68.9 mV dec^{-1}), revealing the fast HER kinetics on the surface of the β-PdHene aerogels follows a Volmer-Tafel mechanism in the acid conditions. Such a phenomenon demonstrates that interstitial lattice hydrogen has a significant role in

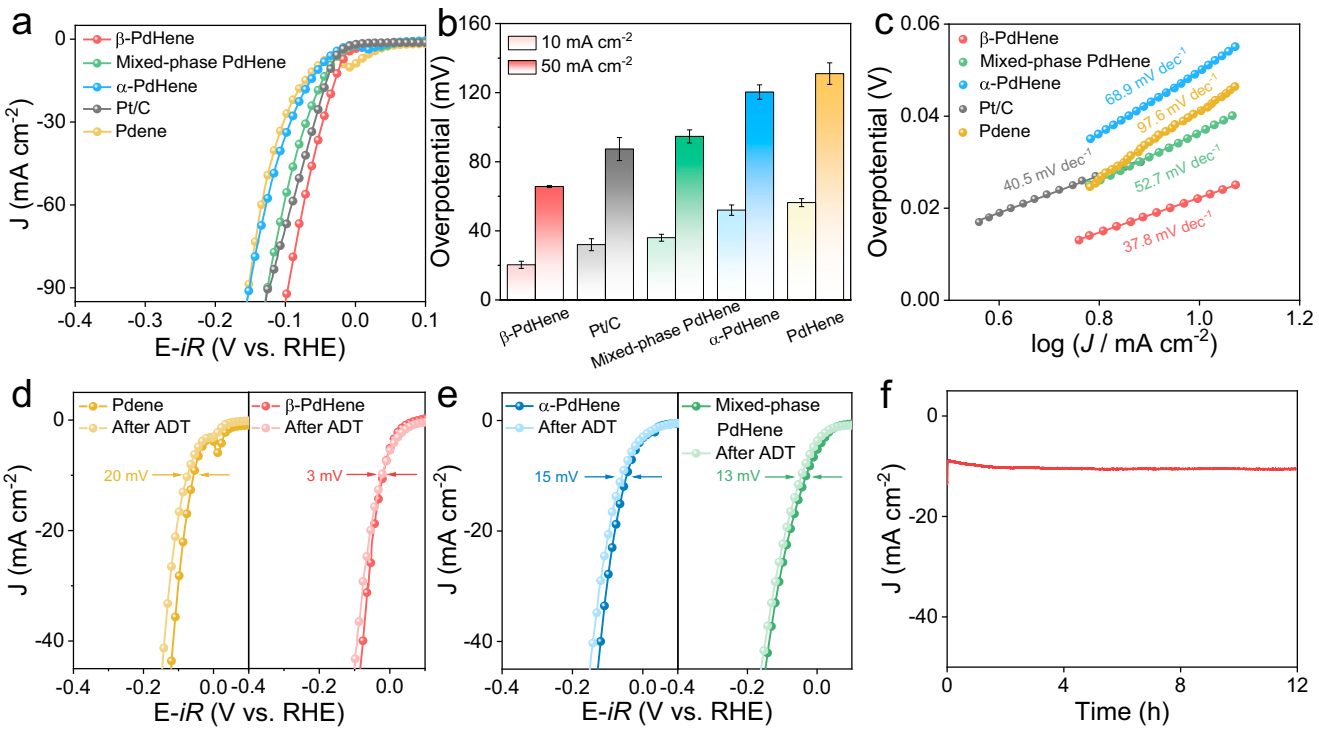

Fig. 2 | Electrocatalytic HER performance. a LSV polarization curves in 0.5 M H_2SO_4 solution, (**b**) Overpotentials at different current densities, and (**c**) Tafel plots of different electrocatalysts (the catalyst loading is 0.14 mg_{Pd} cm^{-2}, the electrode surface area was 0.196 cm^2, the pH of the 0.5 M H_2SO_4 electrolyte is 0.42 ± 0.1, scan rate is 5 mV s^{-1}, rotation rate is 1600 rpm, the resistance is 6.42 ± 0.16 Ω, and temperature is 25 °C). The non-*iR* correction polarization curves were provided in Supplementary Fig. S9. **d**, **e** LSV polarization curves of Pdene and different PdHene aerogels on carbon paper measured before and after 5000 potential cycles (the catalyst loading is 0.14 mg_{Pd} cm^{-2}, the carbon paper electrode surface area is 1 cm^2, the pH of the 0.5 M H_2SO_4 electrolyte is 0.42 ± 0.1, scan rate is 5 mV s^{-1}, rotation rate is 1600 rpm, the resistance is 2.22 ± 0.22, and temperature is 25 °C). **f** CA test of β-PdHene on carbon paper under static overpotential of 20 mV (the catalyst loading is 0.14 mg_{Pd} cm^{-2}, the carbon paper electrode surface area is 1 cm^2, the pH of the 0.5 M H_2SO_4 electrolyte is 0.42 ± 0.1, and temperature is 25 °C). The error bars represent the standard deviation of three independent measurements. Source data for Fig. 2 are provided as a Source Data file.

enhancing HER performance, endowing β-PdHene aerogels as one of the most effective noble metal-based HER electrocatalysts (Supplementary Fig. S10 and Supplementary Table S2). In addition to the electrocatalytic activity, the stability of β-PdHene aerogels also needs to be considered to evaluate the practical application potential. The β-PdHene aerogels also suggest remarkable cycling and long-term stability, which are assessed by the electrochemical accelerated durability test (ADT) and chronoamperometric (CA) test. The HER performance of β-PdHene aerogels displays a negligible positive shift of only 3 mV after ADT of 5000 cycles, while Pdene and commercial Pt/C attenuates 20 mV and 5 mV, respectively (Fig. 2d and Supplementary Fig. S11). In contrast, the overpotential is decreased by 15 mV and 13 mV after ADT for α-PdHene and mixed-phase PdHene aerogels, respectively (Fig. 2e). Furthermore, there is almost no loss of the current density for β-PdHene aerogels after 12 h of the CA test (Fig. 2f). The β-PdHene aerogels still maintain the initial morphology and hydride structure after the ADT and CA tests (Supplementary Figs. S12, S13 and Table S3). All the evidence shown above implies that the β-PdHene aerogels can act as an ideal candidate for HER electrocatalysis in practical applications.

Hydrogen adsorption and desorption behavior of different catalysts

To further understand the significant role of lattice hydrogen for different phases of PdHene aerogels, a series of electrochemical measurements were conducted. The hydrogen adsorption kinetics was carried out by *operando* electrochemical impedance spectroscopy (EIS) measurement on Pdene and different phases of PdHene aerogels at different overpotentials (Fig. 3a and Supplementary Fig. S14). A double-parallel equivalent circuit model was simulated by the obtained Nyquist plots. As listed in Supplementary Table S4, R_s corresponds to the uncompensated solution resistance[27]. All electrocatalysts disclose comparable R_s during the HER process. The parallel components T and R_1 reflect the double-layer capacitance and catalytic charge transfer resistance[28]. Moreover, the values of R_1 of β-PdHene aerogels are smaller than those of other electrocatalysts, thus enabling rapid kinetics for HER. The second parallel component C_φ and R_2 represents the hydrogen adsorption pseudocapacitance and resistance on the surface of catalysts, respectively[29]. Owing to the potential-dependent R_2 for these electrocatalysts, plotting logR_2 vs overpotential and corresponding the EIS-derived Tafel slopes under Ohm's law can estimate the hydrogen adsorption kinetics[30]. Comparatively, the EIS-derived Tafel slopes of β-PdHene aerogels are significantly increased, indicating that the hydrogen adsorption kinetics slows down (Fig. 3b). To explore the hydrogen desorption behavior, the *operando* CV tests of Pdene and different phases of PdHene aerogels were determined. The hydrogen desorption peak is positively shifted with an increment in the scan rate (Fig. 3c and Supplementary Fig. S15)[31]. Therefore, plotting the hydrogen desorption peak position vs the scan rate was employed to compare the fitting slopes, which is logical to quantify the hydrogen desorption kinetics[32]. The declined slope of β-PdHene aerogels exhibits its drastically enhanced hydrogen desorption kinetics (Fig. 3d). Thus, the significantly boosted HER activity on β-PdHene aerogels can be ascribed to the rapid H_2 desorption. Furthermore, the kinetic isotope effects (KIEs) experiment was utilized to investigate hydrogen or proton transfer kinetics behavior. The LSV curves and corresponding KIE values (J_{H_2O}/J_{D_2O} at −0.3 V vs RHE) are obtained in 0.5 M H_2SO_4/H_2O and 0.5 M D_2SO_4/D_2O electrolyte. It is known that the presence of KIE (KIE > 1) is inferred as a descriptor of

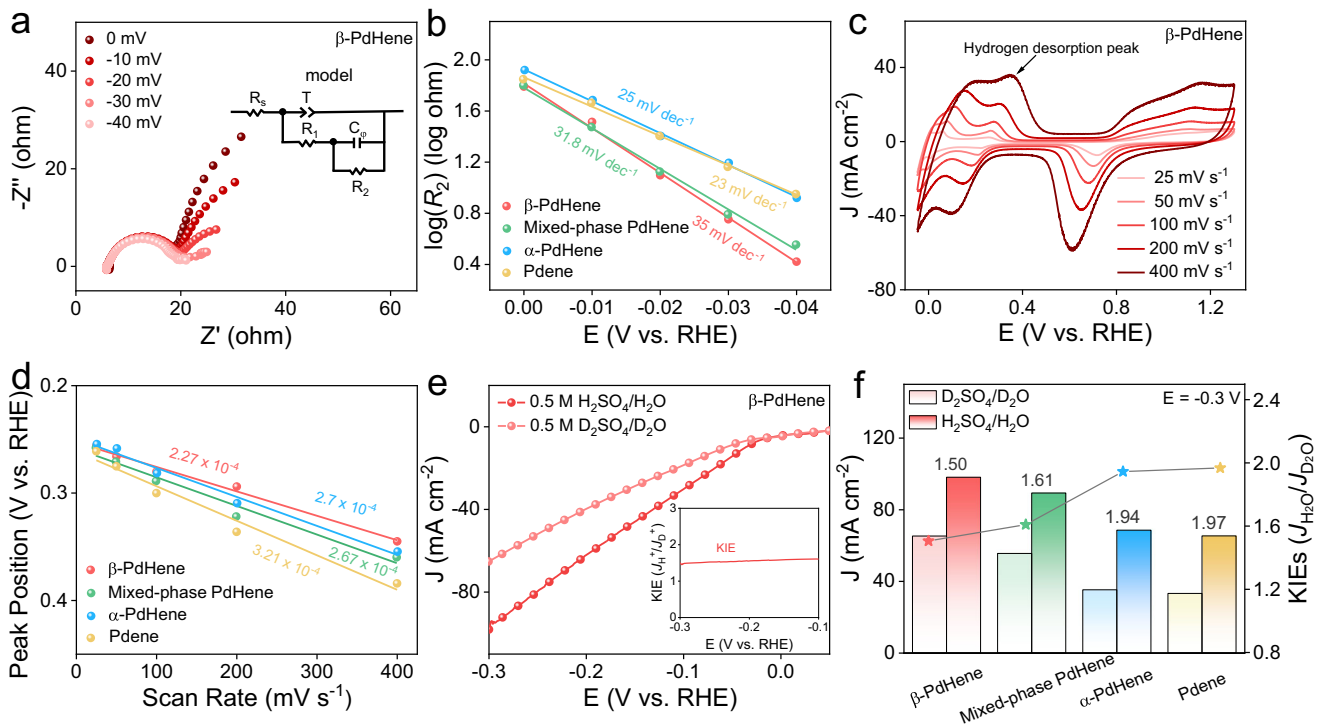

Fig. 3 | Hydrogen adsorption and desorption behavior of different catalysts. **a** Nyquist plots for β-PdHene aerogels at various HER overpotentials. Inset in **a** shows a simulated equivalent circuit. **b** EIS-derived Tafel plots of Pdene and different phases of PdHene aerogels obtained from the hydrogen adsorption resistance R_2. **c** CV curves of β-PdHene aerogels with the scan rate from 25 mV s^{-1} to 400 mV s^{-1} in N_2-saturated 0.5 M H_2SO_4. **d** Plots of hydrogen desorption peak position vs scan rates of Pdene and different phases of PdHene aerogels. **e** LSV polarization curves without *iR* correction of β-PdHene aerogels in 0.5 M H_2SO_4/H_2O and 0.5 M D_2SO_4/D_2O solution. Inset in **e** shows corresponding KIE values plotted against potential. **f** KIE values of H/D over Pdene and different phases of PdHene aerogels at −0.3 V vs RHE. (The catalyst loading is 0.14 mg_{Pd} cm^{-2}, the electrode surface area was 0.196 cm^2, the pH of the 0.5 M H_2SO_4 electrolyte is 0.42 ± 0.1, the scan rate is 5 mV s^{-1}, the rotation rate is 1600 rpm and temperature is 25 °C) Source data for Fig. 3 are provided as a Source Data file.

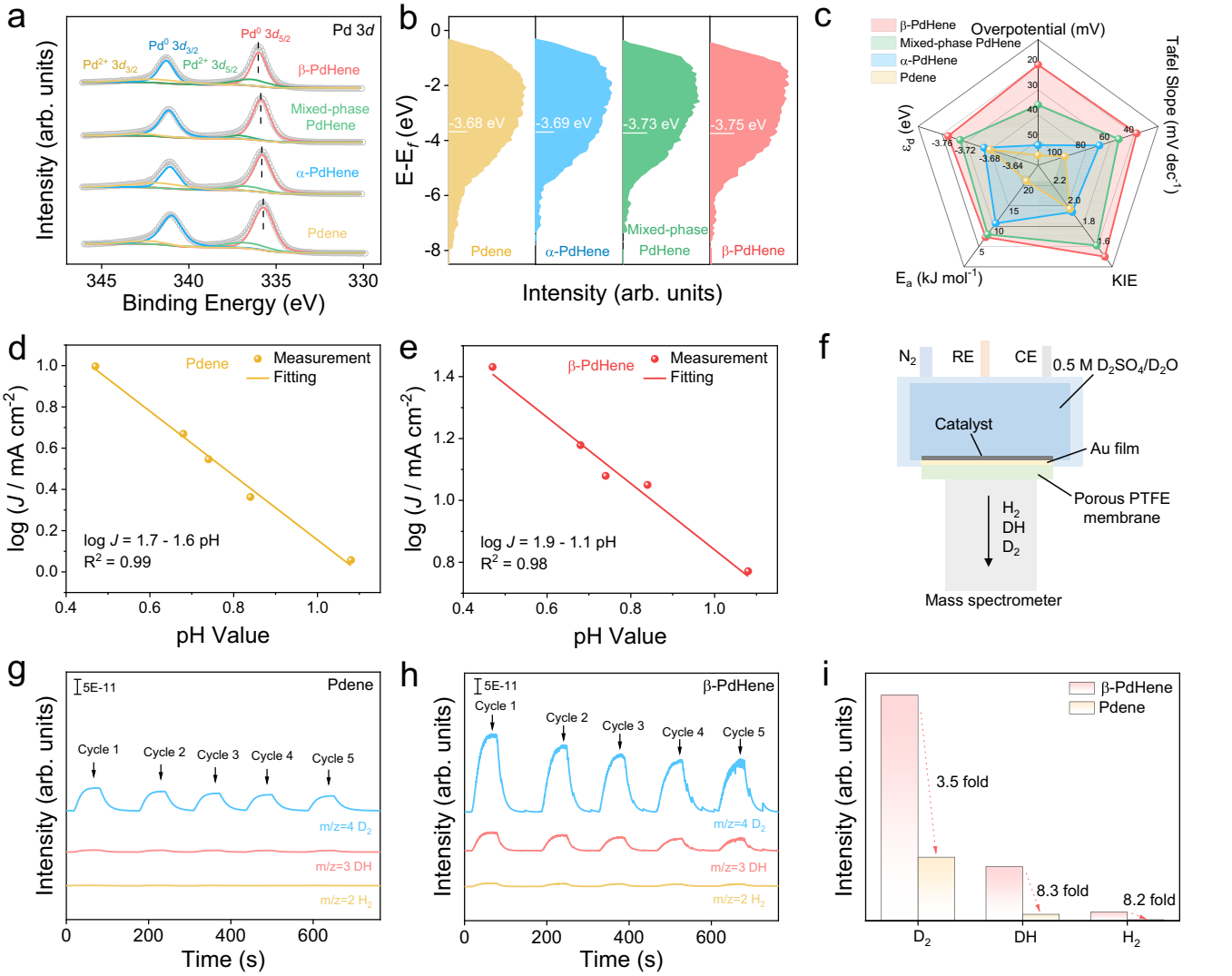

Fig. 4 | Investigation of the reaction mechanism. a Pd 3*d* XPS spectra, (**b**) XPS valence band spectra, and (**c**) the radar map of performance assessment of Pdene and different phases of PdHene aerogels. Plots of log *J* at −0.09 V (vs RHE) vs pH for Pdene (**d**) and β-PdHene catalysts (**e**). **f** Schematic illustration of the in situ DEMS. DEMS signals at $m/z = 2$, 3, and 4 in 0.5 M D_2SO_4/D_2O solution of Pdene (**g**) and β-PdHene (**h**). **i** Histogram of the generated D_2, DH, and H_2 over Pdene and β-PdHene for the fifth cycle during the in situ DEMS test (the catalyst loading is 0.016 mg_{Pd} cm^{-2}, the working electrode area is 0.5 cm^2, and temperature is 25 °C). Source data for Fig. 4 are provided as a Source Data file.

the hydrogen or proton transfer rate affecting the rate-determining step for all electrocatalytic reactions[33]. The HER performance of β-PdHene aerogels is significantly lower in 0.5 M D_2SO_4/D_2O electrolyte compared to that in β-PdHene in the 0.5 M H_2SO_4/H_2O electrolyte by a factor of about 1.50–1.61 (KIEs = 1.50–1.61) within the selected potential range (Fig. 3e), suggesting that the hydrogen or proton transfer is indeed evolved in the rate-determining step. Specifically, the KIE value of β-PdHene is 1.50 at −0.3 V_{RHE}, which is lower than those of Pdene (1.97), α-PdHene (1.94), and mixed-phase PdHene aerogels (1.61), verifying that rapid hydrogen or proton transfer rate (Fig. 3f and Supplementary Fig. S16)[34].

Investigation of the reaction mechanism

The surface electronic structure of Pd in the Pdene and different phases of PdHene aerogels was performed by XPS in Fig. 4a. The Pd 3*d* XPS spectra show that Pd in all metallene materials exists in the metallic state[35,36]. With the introduction of more interstitial lattice hydrogen, the peak position of Pd^0 $3d_{5/2}$ and Pd^0 $3d_{3/2}$ is shifted to higher binding energies compared to that of Pdene. Specifically, Pd 3*d* peaks of β-PdHene show more positive shifts of 0.3 eV than that of Pdene, suggesting the stronger electronic interaction of Pd and H and ultimately resulting in more electron transfer[37–39]. The average energy of the *d*-band center (ε_d) is considered evidence to describe the binding ability between the reaction intermediate and electrocatalysts. The surface valence band spectra analysis verifies that β-PdHene owns the lowest ε_d position based on Eq. 5 (Fig. 4b). Therefore, introducing more interstitial lattice hydrogen to Pdene accelerates the H_2 desorption, beneficial for the reaction kinetics of HER. The temperature-dependent HER kinetic analysis was also carried out in the temperature range of 298–338 K. The thermodynamic HER activation energy is calculated according to the Arrhenius equation based on the current density at −0.05 V vs RHE. The β-PdHene shows that the activation energy is only 7.3 kJ mol^{-1}, which is about 1/3 of that for Pdene (21.1 kJ mol^{-1}), suggesting a significant enhancement in HER kinetics due to the introduction of lattice hydrogen (Supplementary Figs. S17 and 18). The radar map further visually and comprehensively evaluates the good performance of β-PdHene aerogels (Fig. 4c). Currently, it has been reported that lattice hydrogen in Pd hydride is involved in electrochemical reactions, such as nitrogen reduction reaction, but the

involvement of lattice hydrogen during HER have rarely been studied[40]. The reaction mechanism was further revealed by the pH-dependent HER (Fig. 4d, e and Supplementary Fig. S19). The reaction order of 1.6 for the Pdene catalysts is close to the theoretical value of 2 for the traditional HER pathway, which is larger than that of β-PdHene (1.1), suggesting the participation of lattice hydrogen. To further prove the involvement of lattice hydrogen, in situ DEMS with isotope labeling tests was conducted in 0.5 M D_2SO_4/D_2O electrolyte (Fig. 4f). Initially, the Pdene and β-PdHene catalysts are supported on a porous Au-coated polytetrafluoroethylene (PTFE) film as working electrodes and subjected to five consecutive cycles. The mass signal of the HER gaseous product of Pdene and β-PdHene was measured. The $m/z = 4$ signal from D_2 is the strongest for the Pdene electrocatalyst, followed by the $m/z = 3$ and $m/z = 2$ signals from DH and H_2, respectively (Fig. 4g). Since a trace amount of H remains in 0.5 M D_2SO_4/D_2O, the weak signals of DH and H_2 appear. A similar signal trend was also observed on β-PdHene (Fig. 4h). Among them, the D_2 signal is over 3.5 fold than that of Pdene. Moreover, the DH and H_2 signals of β-PdHene are approximately 8.3 fold and 8.2 fold than those of Pdene, respectively (Fig. 4i). Impressively, the increase of DH and H_2 signals is significantly greater than the increase of the D_2 signal, which unambiguously demonstrates the engagement of lattice hydrogen during HER.

DFT calculations

Such a significant improvement of high HER activity of β-PdHene was also unveiled by DFT calculations. According to the above catalyst characterization, the (111) surface models of β-PdH and Pd were constructed and the optimized structure is shown in Supplementary Data 1, Supplementary Figs. S20a and S21a. The 2D slice of electron density difference was calculated to identify the electron transfer ability during the H* adsorption process. As shown in Fig. 5a, the stronger electron depletion of Pd (red color) on β-PdH (111) was obvious in comparison to that of Pd (111). Meanwhile, β-PdH presents a longer Pd–H* bond (1.816 Å) than that of Pd (1.810 Å). These results suggest weakened electron interactions with the introduction of interstitial lattice hydrogen. This point is further confirmed by the results of the projected density of states (PDOS). The results show that the H contributes little to the total density of the state, but affects the Pd *d* orbital to increase the DOS of β-PdHene near the Fermi level in Fig. 5b. The ε_d of β-PdH (−2.12 eV) shows an obvious downshift relative to that of Pdene (−1.88 eV) away from the Fermi level (E_f) in Fig. 5c, revealing that the ε_d is far away from the E_f after the introduction of the interstitial lattice hydrogen. The electronic interaction can be regarded as the coupling between the adsorbate valence states and the metal *d* states, resulting in the generation of separated bonding and antibonding states[41]. Such a downshift of the ε_d will make more electrons occupy antibonding orbitals due to the lower antibonding energy states,

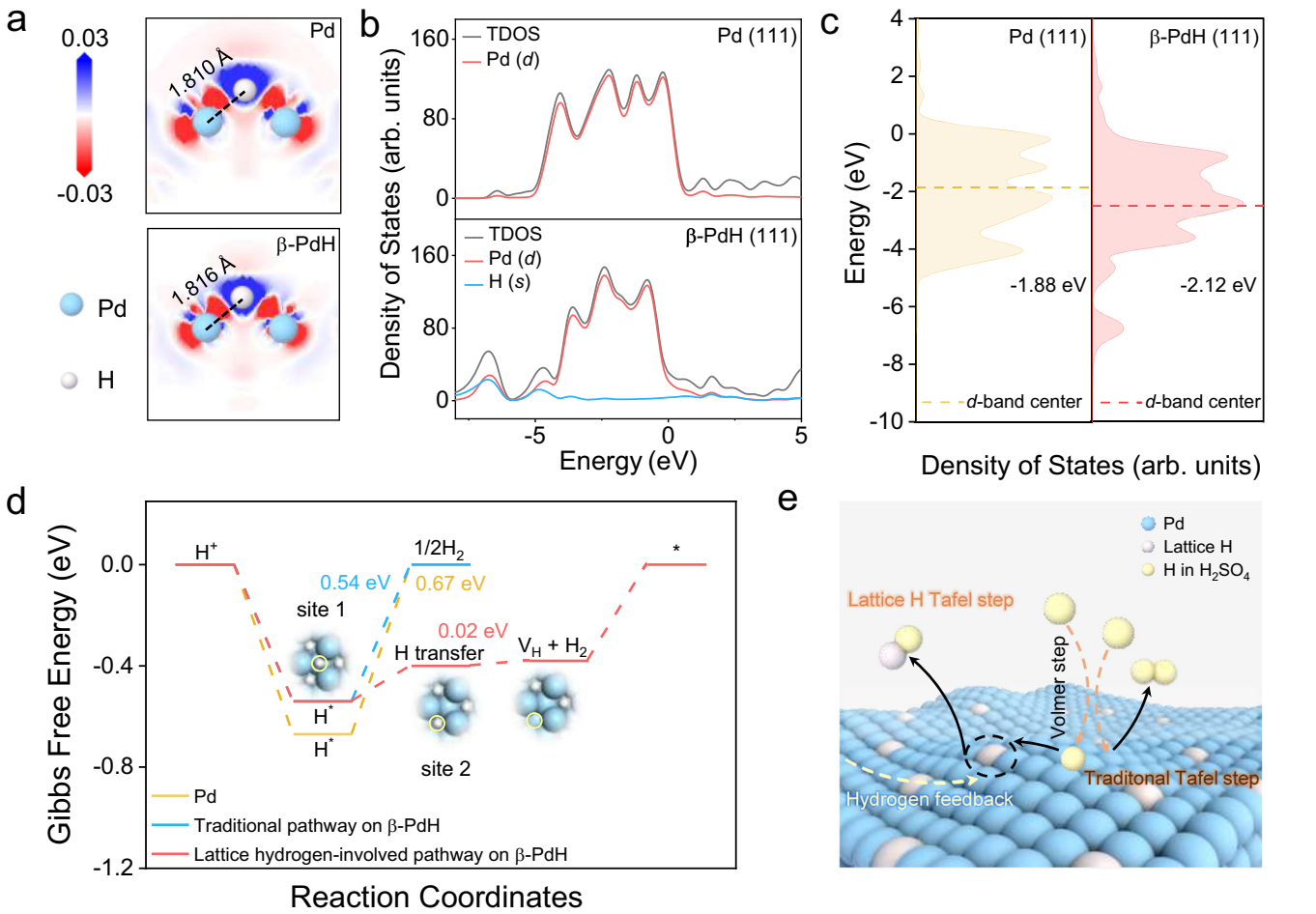

Fig. 5 | DFT calculations. a The 2D electron density difference after H* adsorption on Pd (111) and β-PdH (111) (site 2) for a slice passing along the plane through the Pd–H bond. Red and blue colors represent the depletion and accumulation of electrons, respectively. **b** The total PDOS and (**c**) PDOS diagrams of Pd 3*d* orbitals of Pd (111) and β-PdH (111). **d** Gibbs free energy of HER on the Pd (111) and β-PdH (111) via different reaction pathways. **e** Schematic illustration of the proposed lattice hydrogen-involved mechanism on β-PdHene aerogels. Source data for Fig. 5 are provided as a Source Data file.

further weakening the Pd–H interaction and promoting H_2 desorption. The above phenomenon is consistent with the experimental results. The Tafel slope of β-PdHene presents that HER occurs by the recombination of two H atoms. For the traditional HER pathway, β-PdH possesses the most desirable ΔG_{H^*} of −0.54 eV, which is better than that of Pd (−0.67 eV) (Fig. 5d and Supplementary Figs. S20b and S21b). Additionally, the HER process assisted by lattice hydrogen species is systematically studied. In particular, for the lattice hydrogen-involved pathway, H* on-site 1 experiences an H-transfer to adjacent site 2. As a result, H_2 can be facilely generated with lower energy barriers (0.02 eV) in comparison to the traditional pathway, indicating the key effect of interstitial lattice hydrogen on β-PdH on tuning reaction pathway to improve the HER activity (Supplementary Fig. S21c and d). Thus, a lattice hydrogen-involved mechanism catalyzed by β-PdHene aerogels is proposed following the above experimental and theoretical results (Fig. 5e). Proton in an acid electrolyte initially couples with an electron on the surface by the Volmer step to form an adsorbed H*. Two nearby H* undergo the Tafel step to generate H_2. Adsorbed H* migrates and combines neighboring reactive lattice hydrogen into H_2 is thermodynamically favorable. The hydrogen vacancy state can be eliminated by the fast hydrogen transfer to supply hydrogen, thus achieving the closed loop of the whole catalytic reaction.

Discussion

In summary, an efficient lattice hydrogen-involved mechanism is proposed to separate adsorption and desorption sites on β-PdHene to enhance HER performance in an acidic media, which is preferred energetically over conventional reaction pathways. The direct evidence of lattice hydrogen involvement was confirmed by in situ DEMS experiments and theoretical calculations. The adsorbed H* can migrate and recombine the surrounding lattice hydrogen to generate H_2 molecular via the Tafel step, accelerating the H_2 desorption. The β-PdHene aerogels show enhanced HER activity with a low overpotential (20 mV) at 10 mA cm^{-2} and remarkable long-term electrocatalytic stability. Therefore, our work offers a promising method to design high-performance HER electrocatalysts by the favorable lattice hydrogen participation reaction pathway.

Methods

Reagents

Palladium (II) acetylacetonate ($Pd(acac)_2$, 99.95%, Macklin), Nafion perfluorinated resin solution (5 wt% in a mixture of lower aliphatic alcohols and water, contains 45% water, Macklin), Tungsten hexacarbonyl ($W(CO)_6$, 99%, Macklin), Platinum on graphitized carbon (Pt/C, 20 wt% Pt loading, Aldrich), Deuterated sulfuric acid (D_2SO_4, 96% in D_2O, Aladdin), Deuterium oxide (D_2O, 99.9 at.% D, Meryer), *N*,*N*-DMF (≥99.5%, Sinopharm Chemical Reagent Co., Ltd.), Acetic acid (CH_3COOH, ≥99.5%, Sinopharm Chemical Reagent Co., Ltd.), sulfuric acid (H_2SO_4, 95–98%, Sinopharm Chemical Reagent Co., Ltd.), Deionized water (18.25 MΩ·cm).

Characterization

X-ray diffraction (XRD) characterization was carried out by a D8 ADVANCE (Bruker, Germany). The transmission electron microscope (TEM) was performed from a Tecnai G2 F20 (FEI, USA). The scanning electron microscopy (SEM) was performed from TESCAN MIRA LMS. Supercritical CO_2 drying was conducted using an SPI-Dry™ critical point drying apparatus (SPI Supplies, USA). Atomic force microscopy (AFM) was performed in Multimode8 (Bruker, Germany). The element contents were obtained by inductively coupled plasma mass spectrometry (ICP-MS) (Thermo iCAP RQ). X-ray photoelectron spectroscopy (XPS) measurements were performed by a Thermo Scientific K-Alpha (Thermo Fisher, USA). The specific surface area was determined by N_2 adsorption-desorption on Micromeritics ASAP 2460 instrument.

Synthesis of the β-Pd metallene hydrides (β-PdHene) aerogels

10 mg of $Pd(acac)_2$ and 8 mg $W(CO)_6$ were introduced in 10 mL of CH_3COOH by ultrasonication. The solution was bubbled in a CO flow for 10 min and was then heated at 50 °C. Pdene gels were acquired at the bottom for 1 h. By adding 10 mL DMF, the vial was maintained at 160 °C for 16 h to acquire β-PdHene gels. The α-PdHene and mixed-phase PdHene gels were heated at 120 °C and 140 °C, respectively. Afterward, the corresponding aerogels were obtained by supercritical CO_2 drying.

Electrochemical measurement

All electrochemical tests were performed on a CHI 660E electrochemical workstation. The hydrogen evolution reaction (HER) measurements in acidic media were conducted in a standard three-electrode system electrochemical cell (Pine Research Instrumentation) including a rotating ring-disk electrode (RDE, diameter 5 mm, 0.196 cm^2, Pine Research Instrumentation) as the working electrode, a saturated calomel electrode (Hg/Hg_2Cl_2, SCE) as reference electrode, and graphite rode as the counter electrode, respectively. The preparation of 0.5 M H_2SO_4 electrolyte is as follows: 6.793 mL of concentrated H_2SO_4 (about 18.4 M) is added to a five-compartment electrochemical glass cell containing 243.207 mL of deionized water, and then configured into a solution of H_2SO_4 with a concentration of 0.5 M (pH = 0.42 ± 0.1). The electrolyte is an N_2-saturated 0.5 M H_2SO_4 solution, which is freshly prepared before the electrochemical measurement and stored sealed at 25 °C. The 2.0 mg catalysts and 8.0 mg Cabot carbon black were dispersed in 1.21 mL isopropanol, 1.21 mL deionized water, and 80 µL 5 wt.% Nafion solution to obtain ink by sonication. Then 34.3 µL ink was transferred onto the electrode and dried at 50 °C. The Pd loading is therefore 34.3×10^{-3} mL × 0.8 mg_{Pd}/mL/0.196 cm^2 = 0.14 mg_{Pd} cm^{-2}.

The HER activity of as-prepared catalysts was investigated by linear sweep voltammetry (LSV), which was conducted at a sweeping rate of 5 mV s^{-1}, and a rotational rate of 1600 rpm. Tafel slopes were determined by plotting the overpotential vs the logarithm of current density (log *J*). Electrochemical impedance spectra (EIS) investigations were conducted by using an AC voltage with 5 mV amplitude in the frequency range of 100 kHz–0.1 Hz at various HER overpotentials. The long-term stability was evaluated using the chronoamperometric (CA) test under a static overpotential of 20 mV. The accelerated durability test (ADT) of catalysts was conducted through continuous potential cycling ranging from −0.05 V to 0.05 V vs RHE for 5000 cycles at a scan rate of 100 mV s^{-1}. The calibration of the Hg/Hg_2Cl_2 electrode was carried out in a highly pure saturated hydrogen electrolyte with Pt wire as the working electrode and Pt plate as the counter electrode. The difference between the H^+/H_2 equilibrium potential and the Hg/Hg_2Cl_2 reference electrode is established by identifying the center points of the two potential values associated with zero current on the CV curve. All potentials in this work were calibrated to the RHE using the equation:

$$E_{RHE} = E_{SCE} + 0.252\,V \quad (1)$$

DEMS measurements

In situ DEMS experiments were carried out using a QAS 100 device (Linglu Instruments, Shanghai). A gold-sputtered PolyTetraFluoroEthylene (PTFE) membrane was used as a working electrode substrate (thickness: 40 µm, pore size: ≤20 nm, porosity: ≥50%), in which the PTFE membrane was from Linglu Instruments. The 10 µL

catalyst inks (0.8 mg_{Pd}/mL) were added onto the Au-sputtered PTFE membrane (working area: 0.5 cm^2) and dried at room temperature to form a uniform layer with a loading of 0.016 $mg_{Pd}\,cm^{-2}$. The electrochemical cell is a typical three-electrode system. A $Hg/HgCl_2$ electrode and graphite rode were employed as the reference and counter electrode, respectively. The electrolyte used for in situ DEMS measurements is N_2 saturated 0.5 M D_2SO_4/D_2O, and the volume is 2 mL. Then, five consecutive cycles at the potentiostatic process at −28 mV vs RHE were applied. The gaseous products were pumped into a mass spectrometer and the signal with the mass-to-charge ratio of 2, 3, and 4 could be collected.

Calculation of the lattice hydrogen atoms

$$d = \frac{\lambda}{2\mathrm{Sin}\theta} \tag{2}$$

$$d_{hkl} = \frac{a_0}{\sqrt{h^2 + k^2 + l^2}} \tag{3}$$

$$\frac{3 \times (a_{PdH} - a_{Pd})}{x \times a_{PdH}} = 0.19 \tag{4}$$

Where λ is the wavelength (0.154 nm), θ is the angle, {*hkl*} is the face plane of Pd, a_0 is the lattice constant, and x is the number of hydrogen atoms.

Calculation of the *d*-band centers

The εd was calculated based on the following Equation[42–44].

$$\varepsilon_d = \frac{\int N(E)EdE}{\int N(E)dE} \tag{5}$$

Where *N(E)* is the density of states or intensity of photoelectron spectra after Shirley background correction.

Computational methods

All the calculations are conducted in the CASTEP module of Materials Studio by the plane-wave pseudo-potential method[45]. The generalized gradient approximation (GGA) with ultrasoft pseudopotentials based on the Perdew–Burke–Ernzerhof (PBE) function was employed to handle the exchange-correlation effects[46]. The supercell composed of a 4 × 4 unit with a (111) surface was constructed with a vacuum layer of 15 Å to isolate the periodic unit cell. For the optimization process, the top layer was allowed to relax and the other two layers were fixed. The Monkhorst–Pack *k*-point was 3 × 3 × 1 and the cut-off energy was set as 400 eV. The convergence tolerance energy was 10^{-6} eV/atom and the max force was 0.03 eV/Å. The adsorbed energy ΔE_H was presented by Eq. 6[47].

$$\Delta E_H = E_{H^*} - (E^* + E_H) \tag{6}$$

Where E_{H^*}, E*, and E_H are the H adsorption energy on the substrates, the bare substrates, and the half energy of H_2 gas.

The Gibbs free energy profiles were represented by:

$$\Delta G = \Delta E + \Delta ZPE - T\Delta S \tag{7}$$

Where ΔE, ΔZPE, and $T\Delta S$ are adsorption energy, the difference of zero-point vibrational energy, and the difference of entropy at 298.15 K before and after adsorption.

The electron density difference is defined by Eq. 8:

$$\Delta\rho = \rho_{H@slab} - (\rho_H + \rho_{slab}) \tag{8}$$

where $\rho_{H@slab}$, ρ_H, and ρ_{slab} are the electron densities of the adsorbed H on the slab, the adsorbed H atom, and the clean slab. The 2D electron density difference was obtained for a slice passing along the plane through the Pd–H bond.

Data availability

The data supporting the findings of this study are available within the article and its Supplementary Information files. All other data are available from the corresponding author upon request. Source data are provided with this paper.

References

1. Chen, J. et al. Reversible hydrogen spillover in Ru–WO_{3-x} enhances hydrogen evolution activity in neutral pH water splitting. *Nat. Commun.* **13**, 5382 (2022).
2. Fan, J. et al. Interstitial hydrogen atom modulation to boost hydrogen evolution in Pd-based alloy nanoparticles. *ACS Nano* **13**, 12987–12995 (2019).
3. Zhu, S. et al. The role of ruthenium in improving the kinetics of hydrogen oxidation and evolution reactions of platinum. *Nat. Catal.* **4**, 711–718 (2021).
4. Shi, Z. et al. Phase-dependent growth of Pt on MoS_2 for highly efficient H_2 evolution. *Nature* **621**, 300–305 (2023).
5. Kim, J. et al. Theoretical and experimental understanding of hydrogen evolution reaction kinetics in alkaline electrolytes with Pt-based core-shell nanocrystals. *J. Am. Chem. Soc.* **141**, 18256–18263 (2019).
6. Fan, J. et al. Hydrogen stabilized RhPdH 2D bimetallene nanosheets for efficient alkaline hydrogen evolution. *J. Am. Chem. Soc.* **142**, 3645–3651 (2020).
7. Wan, C. et al. Amorphous nickel hydroxide shell tailors local chemical environment on platinum surface for alkaline hydrogen evolution reaction. *Nat. Mater.* **22**, 1022–1029 (2023).
8. Tan, H. et al. Engineering a local acid-like environment in alkaline medium for efficient hydrogen evolution reaction. *Nat. Commun.* **13**, 2024 (2022).
9. Fan, J. et al. Ligand-confined two-dimensional rhodium hydride boosts hydrogen evolution. *Matter* **6**, 3877–3888 (2023).
10. Jia, Y. et al. Stable Pd–Cu hydride catalyst for efficient hydrogen evolution. *Nano Lett.* **22**, 1391–1397 (2022).
11. Deng, K. et al. Surface engineering of defective and porous Ir metallene with polyallylamine for hydrogen evolution electrocatalysis. *Adv. Mater.* **34**, 2110680 (2022).
12. Wu, J. et al. Atomically dispersed MoO_x on rhodium metallene boosts electrocatalyzed alkaline hydrogen evolution. *Angew. Chem. Int. Ed.* **61**, e202207512 (2022).
13. Yu, H. et al. Defect-rich porous palladium metallene for enhanced alkaline oxygen reduction electrocatalysis. *Angew. Chem. Int. Ed.* **133**, 12134–12138 (2021).
14. Xie, H. et al. Weakening intermediate bindings on CuPd/Pd core/shell nanoparticles to achieve Pt-like bifunctional activity for hydrogen evolution and oxygen reduction reactions. *Adv. Funct. Mater.* **31**, 2100883 (2021).
15. Wang, D. et al. Ethanol-induced hydrogen insertion in ultrafine IrPdH boosts pH-universal hydrogen evolution. *Small* **18**, 2204063 (2022).
16. Zheng, X. et al. Tailoring a local acid-like microenvironment for efficient neutral hydrogen evolution. *Nat. Commun.* **14**, 4209 (2023).
17. Chen, X. et al. Revealing the role of interfacial water and key intermediates at ruthenium surfaces in the alkaline hydrogen evolution reaction. *Nat. Commun.* **14**, 5289 (2023).
18. Liu, K. et al. Coherent hexagonal platinum skin on nickel nanocrystals for enhanced hydrogen evolution activity. *Nat. Commun.* **14**, 2424 (2023).

19. Cheng, Y. et al. Rh MoS_2 nanocomposite catalysts with Pt-like activity for hydrogen evolution reaction. *Adv. Funct. Mater.* **27**, 1700359 (2017).
20. Zhu, L. et al. A rhodium/silicon co-electrocatalyst design concept to surpass platinum hydrogen evolution activity at high overpotentials. *Nat. Commun.* **7**, 12272 (2016).
21. Zhao, Z. et al. Synthesis of stable shape-controlled catalytically active β-palladium hydride. *J. Am. Chem. Soc.* **137**, 15672–15675 (2015).
22. Wang, H. et al. PdBi single-atom alloy aerogels for efficient ethanol oxidation. *Adv. Funct. Mater.* **31**, 2103465 (2021).
23. Luo, M. et al. PdMo bimetallene for oxygen reduction catalysis. *Nature* **574**, 81–85 (2019).
24. Fan, J. et al. Spatially confined PdH_x metallenes by tensile strained atomic Ru layers for efficient hydrogen evolution. *J. Am. Chem. Soc.* **145**, 5710–5717 (2023).
25. Xie, M., Zhang, B., Jin, Z., Li, P. & Yu, G. Atomically reconstructed palladium metallene by intercalation-induced lattice expansion and amorphization for highly efficient electrocatalysis. *ACS Nano* **16**, 13715–13727 (2022).
26. Shi, Y. et al. Solution-phase synthesis of $PdH_{0.706}$ nanocubes with enhanced stability and activity toward formic acid oxidation. *J. Am. Chem. Soc.* **144**, 2556–2568 (2022).
27. Wang, H. et al. Pd metallene aerogels with single-atom W doping for selective ethanol oxidation. *ACS Nano* **16**, 21266–21274 (2022).
28. Liu, Y. et al. Unraveling the function of metal-amorphous support interactions in single-atom electrocatalytic hydrogen evolution. *Angew. Chem. Int. Ed.* **61**, e202114160 (2022).
29. Bu, X. et al. Controlling surface chemical inhomogeneity of Ni_2P/$MoNiP_2$/MoP heterostructure electrocatalysts for efficient hydrogen evolution reaction. *Small* **19**, e2304546 (2023).
30. Li, J. et al. A fundamental viewpoint on the hydrogen spillover phenomenon of electrocatalytic hydrogen evolution. *Nat. Commun.* **12**, 3502 (2021).
31. Li, J. et al. Boosting electrocatalytic activity of Ru for acidic hydrogen evolution through hydrogen spillover strategy. *ACS Energy Lett.* **7**, 1330–1337 (2022).
32. Dai, J. et al. Hydrogen spillover in complex oxide multifunctional sites improves acidic hydrogen evolution electrocatalysis. *Nat. Commun.* **13**, 1189 (2022).
33. Liu, X. et al. Diluting the resistance of built-in electric fields in oxygen vacancy-enriched $Ru/NiMoO_{4-x}$ for enhanced hydrogen spillover in alkaline seawater splitting. *Angew. Chem. Int. Ed.* **63**, e202316319 (2024).
34. Zheng, Q. et al. Cobalt single-atom reverse hydrogen spillover for efficient electrochemical water dissociation and dechlorination. *Angew. Chem. Int. Ed.* **63**, e202401386 (2024).
35. Guo, S. et al. Robust palladium hydride catalyst for electrocatalytic formate formation with high CO tolerance. *Appl. Catal. B* **316**, 121659 (2022).
36. Wu, J. et al. Stable bimetallene hydride boosts anodic CO tolerance of fuel cells. *ACS Energy Lett.* **6**, 1912–1919 (2021).
37. Liu, G. et al. Hydrogen-intercalation-induced lattice expansion of Pd@ Pt core-shell nanoparticles for highly efficient electrocatalytic alcohol oxidation. *J. Am. Chem. Soc.* **143**, 11262–11270 (2021).
38. Wang, Z. et al. The PdH_x metallene with vacancies for synergistically enhancing electrocatalytic N_2 fixation. *Chem. Eng. J.* **450**, 137951 (2022).
39. Padavala, S. K. M. & Stoerzinger, K. A. Role of hydride formation in electrocatalysis for sustainable chemical transformations. *ACS Catal.* **13**, 4544–4551 (2023).
40. Xu, W. et al. Nanoporous palladium hydride for electrocatalytic N_2 reduction under ambient conditions. *Angew. Chem. Int. Ed.* **59**, 3511–3516 (2020).
41. Hu, Q. et al. Subnanometric Ru clusters with upshifted D band center improve performance for alkaline hydrogen evolution reaction. *Nat. Commun.* **13**, 3958 (2022).
42. Yang, J. et al. A robust PtNi nanoframe/N-doped graphene aerogel electrocatalyst with both high activity and stability. *Angew. Chem. Int. Ed.* **60**, 9590–9597 (2021).
43. Shi, K., Si, D., Teng, X., Chen, L. & Shi, J. $Pd/NiMoO_4$/NF electrocatalysts for the efficient and ultra-stable synthesis and electrolyte-assisted extraction of glycolate. *Nat. Commun.* **15**, 2899 (2024).
44. Kim, D., Resasco, J., Yu, Y., Asiri, A. M. & Yang, P. Synergistic geometric and electronic effects for electrochemical reduction of carbon dioxide using gold-copper bimetallic nanoparticles. *Nat. Commun.* **5**, 4948 (2014).
45. Zhang, Y. et al. Atomically thin bismuthene nanosheets for sensitive electrochemical determination of heavy metal ions. *Anal. Chim. Acta* **1235**, 340510 (2022).
46. Perdew, J. P., Burke, K. & Ernzerhof, M. Generalized gradient approximation made simple. *Phys. Rev. Lett.* **77**, 3865–3868 (1996).
47. Tang, Q. & Jiang, D.-e Mechanism of hydrogen evolution reaction on 1T-MoS_2 from first principles. *ACS Catal.* **6**, 4953–4961 (2016).

Acknowledgements

The authors gratefully acknowledge the financial support from a start-up fund of Central China Normal University (C.Z.), the Fundamental Research Funds for the Central Universities (nos. CCNU22JC006 and CCNU20TS013) (C.Z.), and the Program of Introducing Talents of Discipline to Universities of China (111 programs, B17019) (C.Z.).

Author contributions

H.W. conceived the idea, conducted the experiments, and wrote the manuscript. Y.Q., Y.W., and C.W. carried out and analyzed DFT calculations. Y.Q., L.L., and Q.F. guided the analysis of the electrochemical test and materials characterization results. L.H. and W.G. participated in the discussion of the data and edited the manuscript. C.Z. supervised the project. All authors discussed the results and assisted during manuscript preparation.

Competing interests

The authors declare no competing interests.

Additional information

Supplementary information The online version contains supplementary material available at https://doi.org/10.1038/s41467-024-54601-7.

Correspondence and requests for materials should be addressed to Chengzhou Zhu.

Peer review information *Nature Communications* thanks Xiaoqiang Cui, Hiroshi Kitagawa, and the other, anonymous, reviewer(s) for their contribution to the peer review of this work. A peer review file is available.